

Original article:

ENHANCING THE EFFICACY OF ALBENDAZOLE FOR
LIVER CANCER TREATMENT USING MESOPOROUS
SILICA NANOPARTICLES: AN *IN VITRO* STUDY

Mohsen Ghaferi^a , Warda Zahra^b , Azim Akbarzadeh^c ,
Hasan Ebrahimi Shahmabadi^{a,*} , Seyed Ebrahim Alavi^{a,*} 

^a Department of Microbiology, School of Medicine, Rafsanjan University of Medical Sciences, Rafsanjan, Iran

^b Nishtar Medical University and Hospital, Multan 60000, Pakistan

^c Department of Pilot Nanobiotechnology, Pasteur Institute of Iran, Tehran, Iran

* **Corresponding authors:** Seyed Ebrahim Alavi and Hasan Ebrahimi Shahmabadi, Department of Microbiology, School of Medicine, Rafsanjan University of Medical Sciences, Rafsanjan, Iran; Postal code: 7717933777, Tel: +983431315043, E-mails: s.ebrahimalavi@gmail.com; ebrahimi@rums.ac.ir

<https://dx.doi.org/10.17179/excli2020-4491>

This is an Open Access article distributed under the terms of the Creative Commons Attribution License (<http://creativecommons.org/licenses/by/4.0/>).

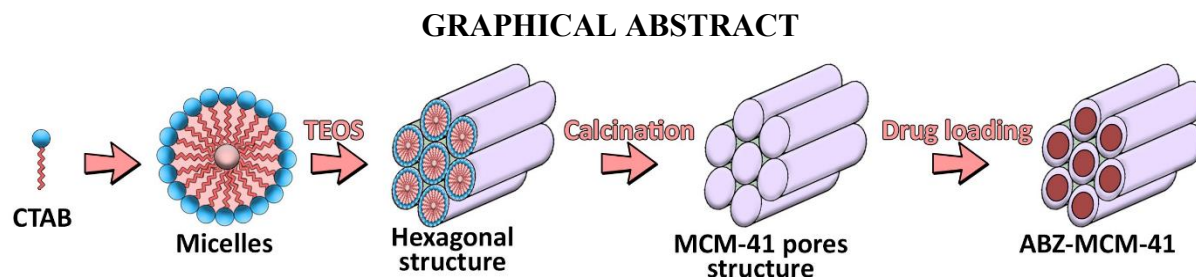


Figure 1: Schematic diagram of the mechanism of albendazole (ABZ)-Mobil Composition of Matter No. 41 (MCM-41) NP synthesis. N-cetyltrimethylammonium bromide (CTAB) is a cationic surfactant micelle and functions as a template for directing the polymerization of silica component (tetraethylorthosilicate; TEOS). The resulting mixture (CTAB+TEOS) is then crystallized under the hydrothermal condition, and the solid product (hexagonal structure) is generated. The solid product is then calcinated to remove CTAB, resulting in the final product (MCM-41 pores structure). The product is then loaded with ABZ, and ABZ-MCM-41 NPs are produced.

ABSTRACT

The present study aimed to synthesize albendazole (ABZ)-loaded Mobil Composition of Matter No. 41 (MCM-41 NPs) to increase the efficacy of the drug against liver cancer. ABZ was loaded into MCM-41 NPs, and after *in vitro* characterization, such as size, size distribution, zeta potential, morphology, chemical composition, thermal profile, drug release, surface and pore volume, and pore size, their biological effects were evaluated using 3-[4,5-dimethylthiazol-2-yl]-2,5 diphenyl tetrazolium bromide (MTT) cell migration assays. The results demonstrated that monodispersed and spherical NPs with a size of 220 ± 11.5 and 293 ± 8.7 nm, for MCM-41 NPs and ABZ-loaded MCM-41 NPs, respectively, and drug loading efficiency of 30 % were synthesized. ABZ was loaded physically into MCM-41 NPs, leading to a decrease in surface volume, pore size, and pore volume. Also, MCM-41

NPs could increase the cytotoxicity effects of ABZ by 2.9-fold ($IC_{50} = 23$ and $7.9 \mu\text{M}$ for ABZ and ABZ-loaded MCM-41 NPs, respectively). In addition, both ABZ and ABZ-loaded MCM-41 NPs could restrain the cell migration by 12 %. Overall, the results of the present study suggest evaluating the potency of MCM-41 NPs, as a potent nanoplatform, for ABZ delivery *in vivo* environment.

Keywords: Albendazole, cancer, drug delivery, MCM-41, mesoporous silica nanoparticles

INTRODUCTION

Liver cancer is the fifth most common cancer and second cancer in terms of mortality in the world (Li et al., 2019b; Momenimovahed and Salehiniya, 2019). The number of new cases and deaths from liver cancer was 841,080 and 781,631, respectively, in 2018 (Bray et al., 2018). Liver cancer has a poor prognosis, mainly due to the diagnosis in many cases is made late or inaccurate (IARC, 2022; Jiao et al., 2019; Marzbani et al., 2019). The five-year survival rate in liver cancer is poor and is less than 20 % (Fang et al., 2017). Moreover, the recurrence rate of liver cancer following surgery is high equal to 70-80 % (De Cicco et al., 2019; Du et al., 2014). Various types of treatment have been used for liver cancer, including surgical resection and chemotherapy (Rabinel et al., 2017).

Albendazole (ABZ) is a benzimidazole carbamate with anthelmintic activity. It functions through targeting and destruction of the β -tubulin structure to restrain the microtubule polymerization (Liu et al., 2020). Recent studies have demonstrated that ABZ can restrain microtubule polymerization, and this can cause anti-tumor activity against various tumors, such as liver cancer (Liu et al., 2020; Pourgholami et al., 2001). Moreover, scientists have demonstrated that ABZ can cause a significant decrease in the activity of hypoxia-inducible factor-1 α (HIF-1 α) and vascular endothelial growth factor (VEGF) in ovarian cancer that restrains tumor angiogenesis, and as a result, decreasing the symptoms of ascites (Noorani et al., 2015). ABZ has also been found as a radiosensitizer in tumor models (e.g., metastatic melanoma and small cell lung cancer) as it can induce DNA damage (Patel et al., 2011).

Despite the wide range of applications, the use of ABZ is restricted owing to low water solubility ($2.7 \mu\text{M}$), which leads to negligible or variable bioavailability following administration (Deodhar et al., 2017). Many efforts have been made to overcome this barrier, such as the use of various solvents (Ibrahim et al., 2020), solid dispersion (Maleki et al., 2017), and microparticles and nanoparticles (NPs). Among all of these strategies, the most successful ones are developing the formulations of ABZ using nanocomplexes and NPs (Deodhar et al., 2017).

NPs are potent to enhance the efficacy of drugs (Alavi and Ebrahimi Shahmabadi, 2021a; Alavi et al., 2013, 2014; Movahedi et al., 2014) and reduce their adverse side effects (Alavi and Ebrahimi Shahmabadi, 2021b; Ghaferi et al., 2020a; Shahabi et al., 2014). Various NPs have been used for the delivery of anticancer drugs (Ebrahimi Shahmabadi et al., 2014; Koochi Moftakhari Esfahani et al., 2014, 2018). In this regard, mesoporous silica NPs (MSNPs) have drawn considerable attention as controlled drug delivery systems (Mahmood et al., 2020).

MSNPs are solid materials containing hundreds of arranged empty mesopores with a high capacity of loading for hydrophobic and hydrophilic drugs (Rahikkala et al., 2018). They are cost-effective nanomaterials with low toxicity, tunable pore size, and simple fabrication method (Li et al., 2019a; Raza et al., 2019). Their surface can be readily functionalized (Deodhar et al., 2017) to improve their cellular uptake. Due to several attractive properties, such as large surface area and pore volume, as well as long regular pore structure, MSNPs are able to improve drug solubility. Also, these carriers, compared to various other polymers utilized to increase

drug solubility, have demonstrated higher thermal resistance, higher levels of resistance to pH, and superior stability on storage. The porous structure of MS materials allows them to confine and stabilize the amorphous state of drug molecules within the pores rather than the crystalline state, resulting in an increase in the solubility rate of the drug molecules (Adrover et al., 2020; Ghaferi et al., 2021). To synthesize MSNPs, a surfactant micelle is used as a template to direct the polymerization of silica components (see graphical abstract, Figure 1) (Mehmood et al., 2017). MSNPs are successfully utilized for oral delivery of hydrophobic drugs, where they can cause an improvement in the dissolution rate and bioavailability of these drugs (Koochi Moftakhari Esfahani et al., 2021a; Tawfeek et al., 2019).

The low water solubility of drugs causes their low absorption, and as a result, their low bioavailability (Chaudhari and Handge, 2020), which, in turn, can lead to a significant decrease in the therapeutic response and an increase in the overall dose (Abu-Huwajj, 2018). ABZ, due to low water solubility, has low bioavailability after oral administration (Pavan Kumar et al., 2007; Savio et al., 1998). The present study aimed to provide a nano-platform of ABZ using MSNPs with an enhanced therapeutic response against liver cancer. For this purpose, ABZ was loaded into the Mobil Composition of Matter No. 41 (MCM-41) NPs, which are high-ordered mesoporous materials (Yao et al., 2001). Next, the *in vitro* characterization of ABZ-loaded NPs was conducted in terms of size, size distribution, zeta potential, morphology, chemical bonds, specific surface area, thermal stability using dynamic light scattering (DLS), scanning (SEM) and transmission (TEM) electron microscopy, Fourier transform-infrared (FT-IR), Brunauer–Emmett–Teller (BET), differential scanning calorimetry (DSC) and thermogravimetric analysis (TGA) methods, respectively. The efficacy of ABZ either in the encapsulated form in MCM-41 NPs or free form was evaluated on HepG2 cells using 3-

[4,5-dimethylthiazol-2-yl]-2,5 diphenyl tetrazolium bromide (MTT) and cell migration assays.

MATERIALS AND METHODS

N-cetyltrimethylammonium bromide (CTAB), dimethylsulfoxide (DMSO), tetraethylorthosilicate (TEOS), acetone, sodium hydroxide (NaOH), phosphate-buffered saline (PBS), MTT, and ABZ were purchased from Merck (Darmstadt, Germany). Roswell Park Memorial Institute (RPMI)-1640 medium, Pen/Strep antibiotics, and fetal bovine serum (FBS) were purchased from Gibco (Waltham, MA, USA). Human liver cancer HepG2 cells were supplied from the Pasteur Institute of Iran (Tehran, Iran).

Synthesis of MCM-41

To synthesize MCM-41 NPs, 1 g of CTAB was added to 480 mL MilliQ water and stirred (700 RPM, room temperature) to obtain a clear solution. Next, NaOH solution (3.5 mL, 2 M) was added (1 mL/min) to the solution, and the mixture was heated to 80 °C using an oil bath under continuous stirring. While heating, 6.7 mL of TEOS was added (1 mL/min) to the mixture, stirred (700 RPM, 2 h), and vacuum filtered. The solution was then washed with MilliQ water three times, and to dry the resulting precipitate, it was put in an oven at 60 °C overnight. The dried precipitate was crushed and heated to 550 °C for 5 h using a muffle furnace to remove any remaining surfactant (CTAB).

Drug loading into MCM-41

Forty milligrams of ABZ were dissolved in 50 mL of acetone using a bath sonicator (50 Hz, 5 min). Next, 160 mg of MCM-41 NPs was added to the mixture and stirred (overnight, room temperature). The organic solvent was then removed using a rotary evaporator (40 °C). The drug-loaded nanoparticles were scratched off from the bottom of the vessel.

Characterization of nanoparticles

Dynamic light scattering

The size, size distribution, and zeta potential of MCM-41 and ABZ-loaded MCM-41 NPs were determined using Zetasizer instrument (Malvern, UK). For this purpose, a suspension of both nanoparticles (100 µg/mL) was provided in PBS (pH 7.4) using a bath sonicator (10 min), and the suspensions were introduced to the instrument.

Transmission electron microscopy

The morphology of ABZ-loaded MCM-41 NPs was studied using TEM (Alavi et al., 2021) (Zeiss, EM10C, 80 kV, Oberkochen, Germany). For this purpose, 20 µL of the nanoparticles suspension was placed on a copper grid and imaged.

Scanning electron microscopy

The morphology of ABZ-loaded MCM-41 NPs was evaluated using SEM XL30 Philips (Eindhoven, The Netherlands) in a high vacuum mode. The nanoparticles were first coated with gold and then evaluated by the SEM instrument.

Fourier transformed infrared spectroscopy

The structure and chemical composition of MCM-41 NPs before and after loading with ABZ were characterized by Fourier-transform infrared spectroscopy (FTIR) (Bruker FRA model 106/5). The KBr tablets with KBr:ABZ, KBr:MCM-41 NPs, and KBr:ABZ-loaded MCM-41 NPs ratio of 100:1 were provided, and the related FTIR spectra were obtained in a frequency range of 400-4000 cm⁻¹.

Thermogravimetric analysis and differential scanning calorimetry

Five milligrams of ABZ, MCM-41 NPs, and ABZ-loaded MCM-41 NPs were characterized in terms of thermal properties and thermal composition using a TGA/DSC Instruments LINSIES STP PT-1000 with a heating rate of 10 °C/min and under an air ambient.

Drug release from nanoparticles

ABZ-loaded MCM-41 NPs (equal to 0.3 mg ABZ) were suspended in 5 mL PBS (pH 1.9 and 7.4) and stirred at 200 RPM at room temperature. At various time intervals (0.25, 0.5, 1, 2, 4, 6, 8, 10, 12 h), 50 µL was taken out and centrifuged. The drug concentrations in the samples were measured using the high-performance liquid chromatography (HPLC) method. Next, the cumulative drug release was calculated using the following equation:

Drug release (%) =

$$\frac{\text{Release drug from particles (mg)}}{\text{Total drug in particles (mg)}} \times 100 \quad (1)$$

The kinetics of the drug release was then determined using mathematical models, including zero-order, first-order, Higuchi and Korsmeyer-Peppas models (Ramezani Farani et al., 2020, 2019).

Brunauer-Emmett-Teller surface area analysis

The total surface area and pore size distribution of MCM-41 NPs before and after loading with ABZ were measured by a surface area and pore size analyzer (BELsorp-mini II, Japan) and Barrett-Joyner-Halenda (BJH) methods. For this purpose, 70 mg of MSNPs and ABZ-loaded MCM-41 NPs were degassed prior to analysis. BET surface area and pore size were then measured by N₂ adsorption using a surface area and pore size analyzer (BELsorp-mini II, Japan).

Biological effects of the nanoparticles

Cytotoxicity studies

The cytotoxicity effects of ABZ-loaded MCM-41 NPs compared to ABZ were evaluated using an MTT assay, as described previously (Alavi et al., 2020). For this purpose, HepG2 cells were cultured in RPMI-1640 medium supplemented with 10 % FBS and 1 % penicillin/streptomycin antibiotics in a 96-well plate at a density of 10⁴ cells/well. After 24 h incubation in a humidified incubator (37 °C, 5 % CO₂), the media were discarded, and the cells were treated with ABZ and

ABZ-loaded MCM-41 NPs at the drug concentrations of 0, 3.1, 6.3, 12.5, 25, 50, and 100 μM prepared from 250 μM stocks of ABZ in 5 % v/v DMSO-water. The plates were incubated (5 % CO_2 , 37 $^\circ\text{C}$) for 24 h, and the media were replaced with MTT solution (100 μL , 0.5 mg/mL PBS). After 4 h incubation (5 % CO_2 , 37 $^\circ\text{C}$), the MTT solution was removed, and 100 μL of DMSO was added to each well to dissolve the formazan crystals. After 20 min incubation (5 % CO_2 , 37 $^\circ\text{C}$), the absorbance was measured at 540 nm using a microplate scanning spectrophotometer (ELISA reader, Organon Teknika, Boxtel, the Netherlands), and the cell viability was measured using the formula below.

Cell viability (%) =

$$\frac{\text{Absorbance}_{\text{sample}} - \text{Absorbance}_{\text{background}}}{\text{Absorbance}_{\text{negative control}} - \text{Absorbance}_{\text{background}}} \times 100 \quad (2)$$

where negative control and background were the treated cells with only media, and only media, respectively. All experiments were performed in triplicate.

Cell migration

To evaluate the effects of the standard ABZ and ABZ-loaded MCM-41 NPs on HepG2 cell migration, the cells were cultured in 12-well plates containing RPMI 1640 medium. At 90-95 % confluency, the scratches were introduced onto the monolayer cell surfaces by a 200 μL sterile pipette tip, and a cell-free area was developed. The cellular debris was removed by gentle washing using a culture medium, and the scratches were imaged (0 h). Next, the media were discarded, and the cells were treated with the standard ABZ and ABZ-loaded MCM-41 NPs at the drug concentrations of 25 μM . The plates were then incubated (5 % CO_2 , 37 $^\circ\text{C}$) for 24 h. The scratches were imaged after 24 h, and their area in each well was measured and analyzed. Finally, the efficacy of ABZ and ABZ-MCM-41 NPs to inhibit cell migration was calculated as a percentage using the following formula:

Cell migration inhibition =

$$\frac{\text{Gap width at time 24 h} - \text{Gap width at time 0}}{\text{Gap width at time 24 h}} \times 100 \quad (3)$$

Statistical analysis

All statistical analyses were performed using GraphPad Prism software version 8.00. ImageJ software (NIH, USA) was used to measure cell migration. Size, size distribution, drug loading efficiency, N_2 adsorption, cell viability data, and cell migration data were expressed as the mean \pm standard deviation (SD, $n = 3$). Statistical differences were analyzed by one-way analysis of variance (ANOVA) test. Statistical analysis was performed using nonlinear regression analysis, and comparisons were made for the half-maximal inhibitory concentration (IC_{50} ; the inhibitory concentration, which causes a decrease of 50 % in cell growth compared with untreated control) values utilizing Tukey's test.

RESULTS AND DISCUSSION

Characterization of nanoparticles

Dynamic light scattering

MCM-41 NPs were successfully synthesized using CTAB, as a precursor, and TEOS, as the silicate source. The synthesized NPs were first characterized in terms of size. The size of NPs is a determinant factor affecting the efficiency of loaded therapeutics in that smaller NPs are more internalized into cells, thereby increasing the intracellular concentration of the loaded therapeutics (Ghaferi et al., 2020b). NPs with a size below 300 nm are efficiently internalized into target cells and exhibit their pharmaceutical effects (Liu et al., 2014). The resulting NPs, in the present study, were found with a size below 300 nm (220 ± 11.5 and 293 ± 8.7 nm, for MCM-41 NPs and ABZ-loaded MCM-41 NPs, respectively, Figure 2a) (Pandey et al., 2018; Tzankova et al., 2019). Also, size distribution is a critical factor that affects various properties of NPs, such as biological effects (Ho, 2014), reproducibility (Syned, 2014), and stability (Dhome

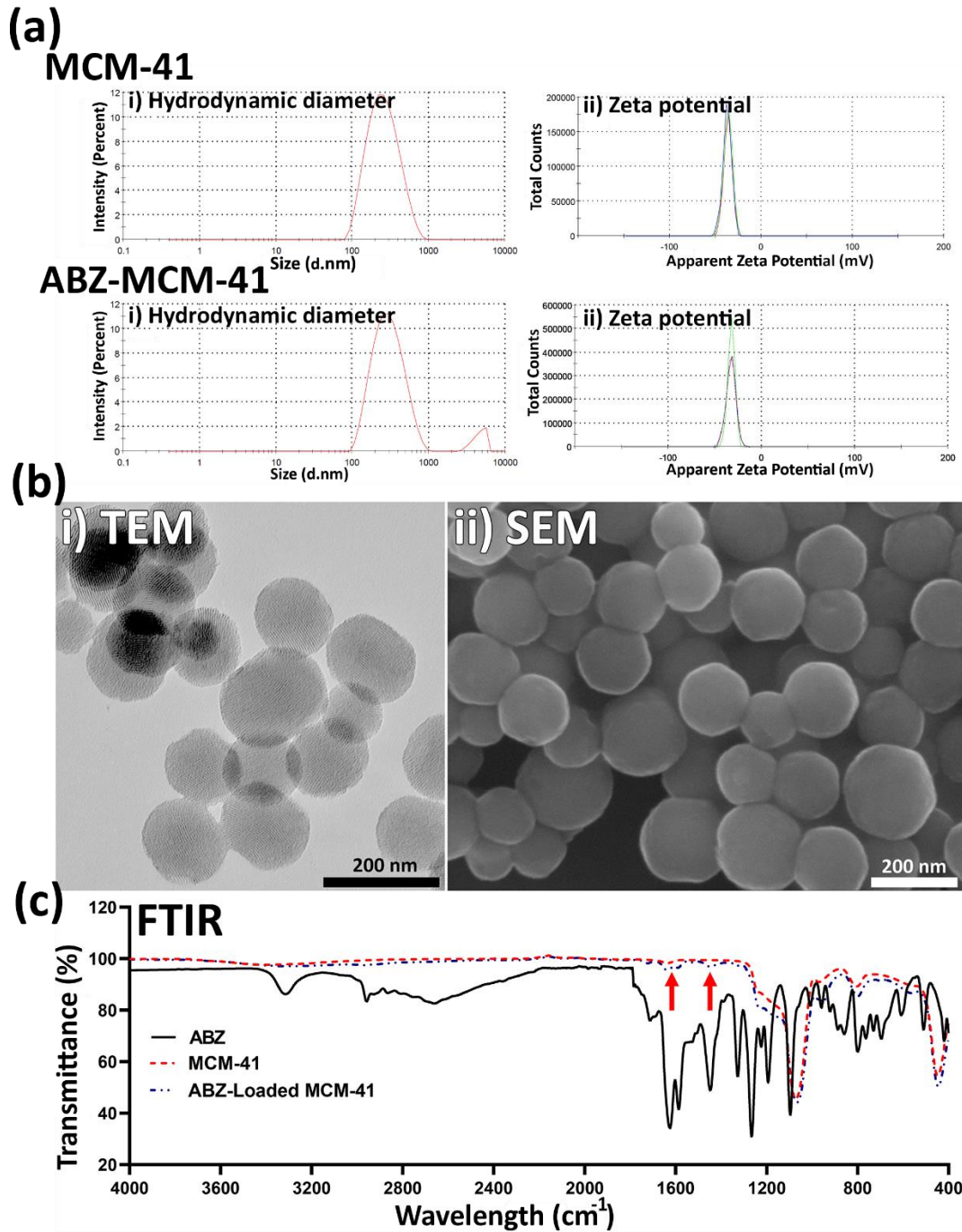


Figure 2: (a) i) Hydrodynamic diameter and ii) zeta potential of Mobil Composition of Matter No. 41 (MCM-41) and albendazole (ABZ)-loaded MCM-41 NPs, measured by the dynamic light scattering (DLS) method. As the results demonstrated, both NP formulations were formed at the nanoscale size (220 ± 11.5 and 293 ± 8.7 nm for MCM-41 and ABZ-loaded MCM-41 NPs, respectively). Also, as the Figure shows, both NPs had negative zeta potential equal to -36.3 ± 4.57 and -33.0 ± 4.93 mV, respectively. (b) i) Transmission electron microscopy (TEM) and ii) scanning electron microscopy (SEM) of ABZ-loaded MCM-41 NPs. As the TEM image demonstrates, mesoporous NPs with a hexagonal array of channels were formed. Also, the SEM image demonstrates that ABZ-loaded MCM-41 NPs were synthesized as homogeneous spheres without any discernible aggregation ($\times 100,000$ mag). (c) Fourier-transform infrared spectroscopy (FTIR) spectra of ABZ, MCM-41, and ABZ-loaded MCM-41 NPs. The peaks related to pure ABZ (e.g., 1623 cm^{-1} , demonstrated by arrows) were observed in the spectrum of ABZ-loaded MCM-41 NPs, confirming that ABZ was loaded into the NPs. Also, as the ABZ-related peaks remained intact in ABZ-loaded MCM-41 NPs, it could be concluded that the drug was loaded into these NPs physically.

et al., 2018). Particles with varying sizes have various properties in terms of i) blood circulation, ii) cellular uptake, and iii) biodistribution (Ho, 2014). Also, increasing the particle size and size distribution can result in the physical instability of NPs (Dhome et al., 2018). The size distribution of MCM-41 and ABZ-loaded MCM-41 NPs were equal to 0.214 and 0.282, respectively, indicating that these NPs were homogenous and monodisperse (He et al., 2020; Honary et al., 2013). Also, the zeta potential of NPs is an important factor to determine the stability of NPs suspension as NPs with the same charge (positive or negative) in aqueous solutions with low ionic strength repulse each other, and this restrains their aggregation (Ghaferi et al., 2020b; Koochi Moftakhari Esfahani et al., 2021b). The zeta potential of MCM-41 and ABZ-loaded MCM-41 NPs were found to be -36.3 ± 4.57 and -33.0 ± 4.93 mV, respectively.

Transmission electron microscopy

TEM was used to evaluate the size and structural features of ABZ-loaded MCM-41 NPs. The results of TEM confirmed the results of DLS and demonstrated that the NPs were synthesized at the nanoscale size. As Figure 2b shows, the NPs were formed in uniform nanospheres. Also, the porous structure of these NPs can be clearly observed.

Scanning electron microscopy

SEM was used to evaluate the surface morphology and size distribution of ABZ-loaded MCM-41 NPs. The SEM image of the NPs demonstrated that these particles were synthesized as homogenous and spherical NPs, which had a smooth surface (Figure 2b). Also, it demonstrated that ABZ-loaded MCM-41 NPs were well dispersed without aggregation.

Fourier Transformed Infrared Spectroscopy

Figure 2c demonstrates the FTIR of pure ABZ. The peak assigned to 3323 cm^{-1} was related to the stretching vibration mode of amide N-H. The absorption band observed at around 2960 cm^{-1} was related to the aliphatic hydrocarbon group (C-H). The ester C=O

bond of the carbamate portion was observed at about 1713 cm^{-1} . The peak related to the aromatic C=C bond was observed at around 1623 cm^{-1} , which along with the amide N-H bond, constitute the benzimidazole portion of the drug. The peak observed at around 1523 cm^{-1} indicated the stretching vibration mode of the C=N group (Adrover et al., 2020). Overall, the FTIR spectrum indicated normal bands of pure ABZ (Adrover et al., 2020). Also, the bands related to asymmetric and symmetric Si-O-Si stretches of MCM-41 were observed at 1110 and 825 cm^{-1} , respectively. A peak at around 980 cm^{-1} was also related to the tension of the Si-OH bonds of the MCM-41 compound (Giraldo et al., 2019). The existence of ABZ related peaks in ABZ-loaded NPs (e.g., 1623 cm^{-1} , demonstrated by arrows in Figure 2c) confirmed that ABZ was loaded into the NPs. According to the results, ABZ preserved its chemical bonds in MCM-41 NPs, indicating the physical loading of ABZ into the NPs.

Thermogravimetric analysis and differential scanning calorimetry

To determine the drug loading efficiency and thermal stability of ABZ, the TGA curves (mass vs. temperature) of ABZ, MCM-41, and ABZ-loaded MCM-41 NPs were measured. According to the results (Figure 3a), an initial weight loss occurred in MCM-41 NPs at around $250\text{ }^{\circ}\text{C}$ due to the evaporation of absorbed water molecules, indicating the hydrophilic nature of this carrier, which is an advantage for loading of poorly water-soluble drugs (Khezri et al., 2014). Also, ABZ-loaded MCM-41 NPs started to be degraded at $150\text{ }^{\circ}\text{C}$ and continued up to $900\text{ }^{\circ}\text{C}$. This resulted in a mass loss of 30 %, which was related to the degradation of ABZ. Based on the results, the amount of ABZ adsorbed onto the NPs was 30 %. ABZ was almost completely degraded at $900\text{ }^{\circ}\text{C}$ (Figure 3a).

DSC analysis can be used to investigate the existence or absence of a crystalline drug (e.g., ABZ) in the pores of mesoporous NPs (Alamdarnjad et al., 2013; Jafari et al., 2016). Also, this method can be used to study the glass transition temperature (T_g) of the

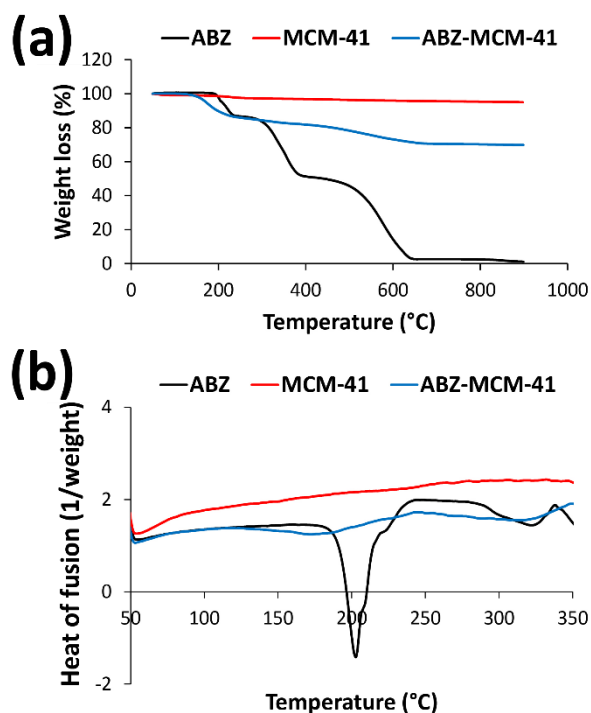


Figure 3: (a) Thermogravimetric analysis (TGA) thermograms of albendazole (ABZ), Mobil Composition of Matter No. 41 (MCM-41), and ABZ-loaded NPs and (b) differential scanning calorimetry (DSC) profiles of ABZ, MCM-41, and ABZ-MCM-41 NPs. Panel a shows, MCM-41 NPs experienced an initial weight loss at 250 °C, resulting in approximately 3 % weight loss. ABZ-loaded NPs were also decomposed at two temperatures, 150 and 450 °C, and this decomposition led to a decrease of 30 % in the mass of the formulation. In addition, ABZ was completely degraded when the temperature reached 900 °C. In panel b, pure ABZ showed a melting endothermic peak around 200 °C, while there were no obvious peaks in the thermogram of MCM-41 NPs. A melting endothermic peak but not sharp was also observed in the thermogram of ABZ-MCM-41 NPs at around 170 °C, which could be attributed to the crystalline anhydrous state of ABZ.

samples, where at the temperature above T_g , various physical properties of a material, such as free molecular volume, heat capacity, thermal expansion coefficient, dielectric coefficient, and viscoelastic features, suddenly change (Bhandari and Howes, 1999; Khezri et al., 2014). Figure 3b illustrates the DSC profiles of the standard ABZ, MCM-41, and ABZ-loaded MCM-41 NPs. As MCM-41 NPs did not have any transitions in the temperature range of 50-350 °C, only the thermal

transition of ABZ was observed (Khezri et al., 2014). Thus, a melting endothermic peak at around 200 °C was observed in the thermogram of ABZ, which is indicative of a crystalline anhydrous state of the drug. Also, the DSC profile of ABZ-MCM-41 demonstrated a melting endothermic peak around 170 °C, which was related to the crystalline anhydrous state of ABZ, confirming drug loading into NPs.

Drug release from nanoparticles

Several daily doses of a drug are needed to attain and preserve the therapeutic concentration of the drug. This might lead to significant fluctuations in the plasma concentration of the drug (Fahr and Liu, 2007), resulting in a decrease in the concentration beyond the minimum effective concentration, or an increase in the concentration above the minimum toxic concentration, and consequently, resulting in the lack of therapeutic effects or unfavorable toxic effects (Ghaferi et al., 2020b). These fluctuations in the plasma drug concentration can be reduced using sustained-release and controlled-release drug delivery systems, leading to improvements in the therapeutic outcome of the drug (Porta-i-Batalla et al., 2016).

In the present study, in order to simulate the pH changes in the gastrointestinal tract, the drug release was evaluated at pH 1.9 and 7.4, corresponding to the pH values of the human stomach (Kavousi et al., 2019) and intestinal fluids (Chen et al., 2008), respectively. The results demonstrated that the release of ABZ from MCM-41 NPs was initiated with a burst release, in which in the first 15 min of the study, 62 and 70 % of the loaded ABZ was released at pH 1.9 and 7.4, respectively (Figure 4). The burst drug release could stem from the release of the adsorbed drug onto the NPs or weakly bound between the drug and the NPs surface (Ghaferi et al., 2020a). In addition, by increasing the surface area of NPs, the amount of initial burst release increased (Alavi et al., 2019). The pattern of the drug release continued with a gradually increasing trend at both pH values, in which 75 and 80 % of the loaded drug were released after 12 h,

indicating a sustained and controlled drug release pattern.

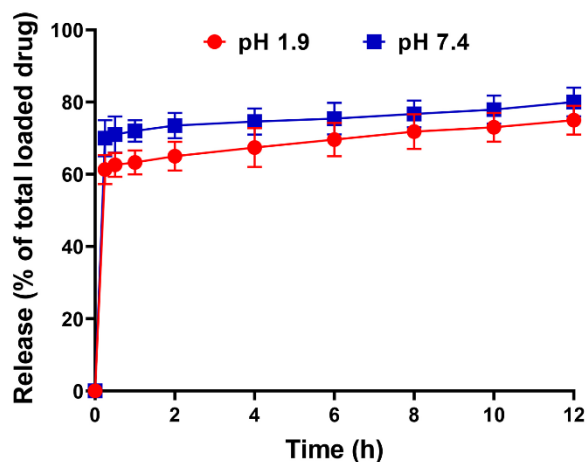


Figure 4: The cumulative percentage of albendazole (ABZ) release versus time from ABZ-loaded Mobil Composition of Matter No. 41 (MCM-41) NPs at pH 1.9 and 7.4. As the results showed, a burst drug release from the NPs occurred at the first 15 min of the study, leading to the release of 62 and 70 % of the loaded drug at pH 1.9 and 7.2, respectively. The release was then continued with a sustained and controlled release in the remaining time of the study. Statistical analyses were performed using one-way analysis of variance (ANOVA) and F-tests. The data are expressed as mean \pm SD ($n = 3$).

Also, according to the results, the drug release was pH-dependent; however, the difference in the amount of the drug release between the two pHs was not statistically significant. These results were approximately similar to the results of Nguyen et al.'s study (2017), where the difference in the amount of drug (prednisolone) release from MSNs at pH 1.9 and pH 7.4 was $\sim 2\%$. In the current study, the difference in the amount of drug release in two pHs could be related to various factors, such as MSNPs agglomeration at acidic pH and variation in the surface charge of the nanoformulation in different pH (Vazhayal et al., 2014; Zeleňák et al., 2018). At acidic pH (pH 1.9), the drug release from the pores of the agglomerated particles is inhibited, resulting in lower drug release (Zeleňák et al., 2018). Also, to determine the kinetics of the drug release, the profiles of

drug release were analyzed using different kinetic models, including zero and first order, Higuchi, and Korsmeyer Peppas models, and the correlation coefficient values were determined for the linear curves. Based on the results, the higher R^2 values (0.3766 and 0.4156 at pH 1.9 and 7.4, respectively) were obtained in the Higuchi model compared to other drug release models; thus, the drug release from the nanoformulation at both pH followed the Higuchi kinetic model.

Brunauer-Emmett-Teller surface area analysis

The N_2 adsorption/desorption isotherms of the calcined MCM-41 and ABZ-loaded MCM-41 NPs are demonstrated in Figure 5. MCM-41 and ABZ-loaded MCM-41 NPs demonstrated the behavior of the mesoporous material and type IV isotherm based on the IUPAC isotherm classification system. These isotherms can be divided into three steps, including i) a linear increase in N_2 adsorption, occurring at relatively low pressure owing to the monolayer adsorption of N_2 on the wall of MCM-41 and ABZ-loaded MCM-41 NPs; ii) capillary condensation of N_2 inside the mesopores, which is indicative of narrow pore size distribution; and iii) saturation step, presented as a long plateau at higher pressures owing to the low N_2 adsorption onto the external surface of the calcined MCM-41 and ABZ-loaded MCM-41 NPs (Khezri et al., 2014). Based on these results, the surface volume for MCM-41 and ABZ-loaded MCM-41 NPs was found to be 540 and 380 m^2/g , respectively, while the pore size for these formulations was found to be 2.5 and 2.1 nm, respectively. In addition, the pore volume of MCM-41 and ABZ-loaded MCM-41 NPs was determined to be approximately 0.75 and 0.46 cm^3/g , respectively.

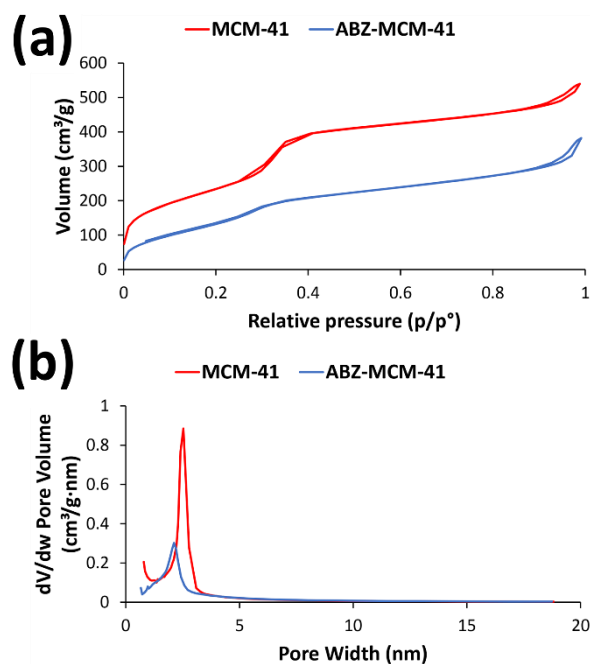


Figure 5: N₂ adsorption/desorption isotherms of Mobil Composition of Matter No. 41 (MCM-41) and albendazole (ABZ)-MCM-41 NPs for measuring their (a) surface volume and (b) pore size. As the results showed, a sharp increase in the N₂ uptake around $p/p^* 0.3$ occurred, which could be attributed to capillary condensation in cylindrical pores of MCM-41 and ABZ-loaded MCM-41 NPs. Also, the surface volume and pore size of the carrier decrease after drug loading. However, this decrease does not affect the mesoporous structure of this carrier.

Biological effects of the nanoparticles

Cytotoxicity studies

The cytotoxicity effects of ABZ, MCM-41, and ABZ-loaded MCM-41 NPs were investigated on HepG2 cells using MTT assay to determine if ABZ loading into NPs caused enhanced cytotoxicity effects or not. For this purpose, ABZ at the concentrations of 0, 3.1, 6.3, 12.5, 25, 50, and 100 μM were used as these concentrations encompass the reported serum concentration of ABZ (4.3 μM), when administered at the standard doses (10 mg/kg/day). Also, a significantly higher drug concentration (100 μM) was used to make the toxicity more pronounced. The results demonstrated that MCM-41 NPs, at the concentration of 25 $\mu\text{g/mL}$, had no toxicity effects on the cells. It was found that ABZ loading into NPs caused a significant increase in

the cytotoxicity effects of the drug in a concentration-dependent manner (Figure 6a), in which the IC₅₀ values for ABZ and ABZ-MCM-41 NPs were estimated 23 and 7.9 μM , respectively.

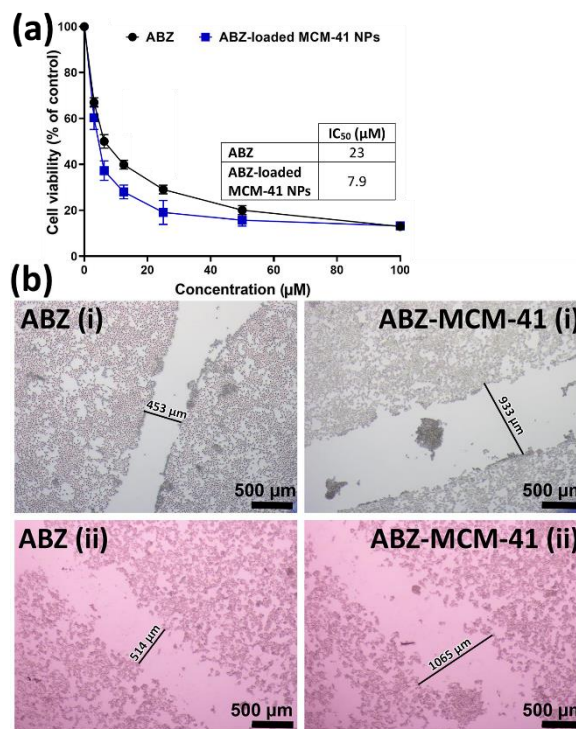


Figure 6: (a) Cell viability effects of albendazole (ABZ) and ABZ-loaded Mobil Composition of Matter No. 41 (MCM-41) NPs on HepG2 liver cancer cells after 24 h. As the Figure demonstrates, the loading of ABZ into MCM-41 NPs caused a significant reduction in HepG2 cell viability compared to that of the standard drug ($P < 0.05$). The data were expressed as mean \pm SD ($n = 3$). (b) Effects of ABZ and ABZ-loaded MCM-41 NPs on the HepG2 cells migration (i) before (0 h) and (ii) after (24 h) cell treatment ($\times 40$ mag). Both ABZ and ABZ-loaded MCM-41 NPs restrained the cell migration by approximately 12 %, confirming the cytotoxicity effects of ABZ and ABZ-MCM-41 NPs.

Cell migration

Migration is a distinctive feature of cellular behavior that contributes to embryogenesis, tissue remodeling, wound healing, and pathologies, such as cancer metastasis and invasion (Glenn et al., 2016; Grada et al., 2017). The cell migration was determined using HepG2 cells at different time intervals to recognize the distance at which cancer cell invasion happened. A scratch was generated and

treated with ABZ and ABZ-loaded MCM-41 NPs at the drug concentration of 25 μ M. The cancer cell migration was monitored by taking pictures at times 0 and 24 h (Figure 6b). As the results demonstrated, both ABZ (gap width of 453 and 514 μ m at times 0 and 24 h, respectively) and ABZ-loaded MCM-41 NPs (gap width of 933 and 1065 μ m at times 0 and 24 h, respectively) inhibited cell migration by approximately 12 %. This indicated that, after loading ABZ with MCM-41 NPs, its potency to inhibit cell migration was unchanged.

CONCLUSION

Poorly water-soluble drugs have low absorption, and consequently, have low bioavailability (Chaudhari and Handge, 2020), which causes a considerable decrease in the therapeutic response and an increase in the overall dose (Abu-Huwajj, 2018). ABZ has poor water solubility, and as a result, has low bioavailability (Savio et al., 1998). MSNPs are able to increase the solubility rate of poorly water-soluble drugs (Adrover et al., 2020; Ghaferi et al., 2021). The present study aimed to increase the efficacy of ABZ against liver cancer cells through loading into MCM-41 NPs. The MCM-41 and ABZ-loaded MCM-41 NPs were successfully synthesized using CTAB as a precursor. The characterization results demonstrated that nanoscale size particles were constructed. Both NPs were monodisperse with high thermal stability. MCM-41 NPs demonstrated high potency for the loading of ABZ (with the drug loading efficiency of 30 %), which is a poorly water-soluble drug. This can cause a significant increase in ABZ solubility and, as a result, drug bioavailability. Also, ABZ-loaded MCM-41 NPs can significantly increase the cytotoxicity effects of ABZ (by 2.6-fold) against liver cancer HepG2 cells. Also, the cell migration results demonstrated that both ABZ and ABZ-MCM-41 NPs could inhibit cancer cell migration by approximately 12 %. Overall, the results of the present study suggest evaluating the efficacy of ABZ-loaded MCM-41 NPs *in vivo* environment.

Authors' contribution

Conceptualization, M.G., S.E.A., A.A. and H.E.S; methodology, W.Z.; software, A.A.; validation, S.E.A. and M.G.; formal analysis, M.G.; investigation, W.Z. and A.A.; writing-original draft preparation, H.E.S. and S.E.A.; writing—review and editing, S.E.A.; visualization, S.E.A.; supervision, S.E.A. and H.E.S.; project administration. All authors have read and agreed to the published version of the manuscript.

Conflict of interest

The authors declare that they have no conflict of interest.

Informed consent

This article does not contain any studies with human participants.

REFERENCES

- Abu-Huwajj RT. Promising polymeric buccoadhesive bilayered tablets releasing valsartan: effect of gel strength. *Jordan J Pharm Sci.* 2018;11:119-31.
- Adrover ME, Pedernera M, Bonne M, Lebeau B, Bucalá V, Gallo L. Synthesis and characterization of mesoporous SBA-15 and SBA-16 as carriers to improve albendazole dissolution rate. *Saudi Pharm J.* 2020;28:15-24.
- Alamdarnjad G, Sharif A, Taranejoo S, Janmaleki M, Kalae MR, Dadgar M, et al. Synthesis and characterization of thiolated carboxymethyl chitosan-graft-cyclodextrin nanoparticles as a drug delivery vehicle for albendazole. *J Mater Sci Mater Med.* 2013; 24:1939-49.
- Alavi SE, Ebrahimi Shahmabadi H. Anthelmintics for drug repurposing: opportunities and challenges. *Saudi Pharm J.* 2021a;29:434-45.
- Alavi SE, Ebrahimi Shahmabadi H. GLP-1 peptide analogs for targeting pancreatic beta cells. *Drug Discov Today.* 2021b;26:1936-43.
- Alavi SE, Koohi Moftakhari Esfahani M, Alavi F, Movahedi F, Akbarzadeh A. Drug delivery of hydroxyurea to breast cancer using liposomes. *Indian J Clin Biochem.* 2013;28:299-302.
- Alavi SE, Koohi Moftakhari Esfahani M, Ghassemi S, Akbarzadeh A, Hassanshahi G. In vitro evaluation of the efficacy of liposomal and pegylated liposomal hydroxyurea. *Indian J Clin Biochem.* 2014;29:84-8.

- Alavi SE, Muflih Al Harthi S, Ebrahimi Shahmabadi H, Akbarzadeh A. Cisplatin-loaded polybutylcyanoacrylate nanoparticles with improved properties as an anticancer agent. *Int J Mol Sci.* 2019;20:1531-44.
- Alavi SE, Cabot PJ, Yap GY, Moyle PM. Optimized methods for the production and bioconjugation of site-specific, alkyne-modified glucagon-like peptide-1 (GLP-1) analogs to azide-modified delivery platforms using copper-catalyzed alkyne-azide cycloaddition. *Bioconjug Chem.* 2020;31:1820-34.
- Alavi SE, Cabot PJ, Raza A, Moyle PM. Developing GLP-1 conjugated self-assembling nanofibers using copper-catalyzed alkyne-azide cycloaddition and evaluation of their biological activity. *Bioconjug Chem.* 2021;32:810-20.
- Bhandari BR, Howes T. Implication of glass transition for the drying and stability of dried foods. *J Food Eng.* 1999;40:71-9.
- Bray F, Ferlay J, Soerjomataram I, Siegel RL, Torre LA, Jemal A. Global cancer statistics 2018: GLOBOCAN estimates of incidence and mortality worldwide for 36 cancers in 185 countries. *CA Cancer J Clin.* 2018;68:394-424.
- Chaudhari SP, Handge NM. Formulation, development and evaluation of lopinavir loaded polymeric micelles. *J Sci Technol.* 2020;5:173-87.
- Chen L, Remondetto G, Rouabhia M, Subirade M. Kinetics of the breakdown of cross-linked soy protein films for drug delivery. *Biomaterials.* 2008;29:3750-56.
- De Cicco P, Catani MV, Gasperi V, Sibilano M, Quaglietta M, Savini I. Nutrition and breast cancer: a literature review on prevention, treatment and recurrence. *Nutrients.* 2019;11:1514-41.
- Deodhar GV, Adams ML, Trewyn BG. Controlled release and intracellular protein delivery from mesoporous silica nanoparticles. *Biotechnol J.* 2017;12:1600408.
- Dhome AG, Deshkar SS, Shirolkar SV. Glioclazide solid lipid nanoparticles: formulation, optimization and in vitro characterization. *Pharm Reson.* 2018;1:8-16.
- Du M, Chen L, Zhao J, Tian F, Zeng H, Tan Y, et al. Microvascular invasion (MVI) is a poorer prognostic predictor for small hepatocellular carcinoma. *BMC Cancer.* 2014;14:38-44.
- Ebrahimi Shahmabadi H, Movahedi F, Koochi Moftakhari Esfahani M, Alavi SE, Eslamifard A, Mohammadi Anaraki G, et al. Efficacy of cisplatin-loaded polybutyl cyanoacrylate nanoparticles on the glioblastoma. *Tumor Biol.* 2014;35:4799-806.
- Fahr A, Liu X. Drug delivery strategies for poorly water-soluble drugs. *Expert Opin Drug Deliv.* 2007;4:403-16.
- Fang Y, Yang W, Cheng L, Meng F, Zhang J, Zhong Z. EGFR-targeted multifunctional polymersomes doxorubicin induces selective and potent suppression of orthotopic human liver cancer in vivo. *Acta Biomater.* 2017;64:323-33.
- Ghaferi M, Amari S, Mohrir BV, Raza A, Shahmabadi HE, Alavi SE. Preparation, characterization, and evaluation of cisplatin-loaded polybutylcyanoacrylate nanoparticles with improved in vitro and in vivo anticancer activities. *Pharmaceuticals.* 2020a;13:44-59.
- Ghaferi M, Asadollahzadeh MJ, Akbarzadeh A, Ebrahimi Shahmabadi H, Alavi SE. Enhanced efficacy of PEGylated liposomal cisplatin: In vitro and in vivo evaluation. *Int J Mol Sci.* 2020b;21:559-74.
- Ghaferi M, Koochi Moftakhari Esfahani M, Raza A, Al Harthi S, Ebrahimi Shahmabadi H, Alavi SE. Mesoporous silica nanoparticles: synthesis methods and their therapeutic use-recent advances. *J Drug Target.* 2021;29:131-54.
- Giraldo L, Rodriguez-Estupiñán P, Moreno-Piraján JC. Isothermic heat: comparative study between Clausius-Clapeyron, CSK and adsorption calorimetry methods. *Processes.* 2019;7:203-27.
- Glenn HL, Messner J, Meldrum DR. A simple non-perturbing cell migration assay insensitive to proliferation effects. *Sci Rep.* 2016;6:31694.
- Grada A, Otero-Vinas M, Prieto-Castrillo F, Obagi Z, Falanga V. Research techniques made simple: analysis of collective cell migration using the wound healing assay. *J Invest Dermatol.* 2017;137:e11-6.
- He Y, Ye Z, Liu X, Wei Z, Qiu F, Li H-F, et al. Can machine learning predict drug nanocrystals? *J Control Release.* 2020;322:274-85.
- Ho DN. Magnetic resonance imaging and alternating magnetic fields. In: Chen X, Wong S (eds): *Cancer theranostics* (pp 255-68). Oxford: Academic Press, 2014.
- Honary S, Barabadi H, Gharaei-Fathabad E, Naghibi F. Green Synthesis of silver nanoparticles induced by the Fungus *penicillium citrinum*. *Trop J Pharm Res.* 2013;12:7-11.
- IARC. Global Cancer Observatory. <http://gco.iarc.fr>. Accessed 27 Sept 2018.

- Ibrahim AH, Smått J-H, Govardhanam NP, Ibrahim HM, Ismael HR, Afouna MI, et al. Formulation and optimization of drug-loaded mesoporous silica nanoparticle-based tablets to improve the dissolution rate of the poorly water-soluble drug silymarin. *Eur J Pharm Sci.* 2020;142:105103.
- Jafari S, Maleki-Dizaji N, Barar J, Barzegar-Jalali M, Rameshrad M, Adibkia K. Physicochemical characterization and in vivo evaluation of triamcinolone acetone-loaded hydroxyapatite nanocomposites for treatment of rheumatoid arthritis. *Colloids Surf B Biointerfaces.* 2016;140:223-32.
- Jiao Y, Li Y, Jiang P, Fu Z, Liu Y. High MAST2 mRNA expression and its role in diagnosis and prognosis of liver cancer. *Sci Rep.* 2019;9:19865.
- Kavousi F, Goodarzi M, Ghanbari D, Hedayati K. Synthesis and characterization of a magnetic polymer nanocomposite for the release of metoprolol and aspirin. *J Mol Struct.* 2019;1183:324-30.
- Khezri K, Haddadi-Asl V, Roghani-Mamaqani H. Introduction of a double bond containing modifier on the surface of MCM-41 nanoparticles: application for SR&NI ATRP of styrene. *Nano.* 2014;9:1450023.
- Koochi Moftakhari Esfahani M, Alavi SE, Akbarzadeh A, Ghassemi S, Saffari Z, Farahnak M, et al. Pegylation of nanoliposomal paclitaxel enhances its efficacy in breast cancer. *Trop J Pharm Res.* 2014;13:1195-8.
- Koochi Moftakhari Esfahani M, Alavi SE, Shahbazian S, Ebrahimi Shahmabadi H. Drug delivery of cisplatin to breast cancer by polybutylcyanoacrylate nanoparticles. *Adv Polym Technol.* 2018;37:674-8.
- Koochi Moftakhari Esfahani MA, Seyed Ebrahim, Cabot PJ, Islam N, Izake EL. PEGylated Mesoporous Silica Nanoparticles (MCM-41): A promising carrier for the targeted delivery of fenbendazole into prostate cancer cells. *Pharmaceutics.* 2021a;13:1605-20.
- Koochi Moftakhari Esfahani M, Islam N, Cabot PJ, Izake EL. Development of thiabendazole-loaded mesoporous silica nanoparticles for cancer therapy. *ACS Biomater Sci Eng.* 2021b; epub ahead of print. DOI 10.1021/acsbomaterials.1c00066.
- Li H, Pan Y, Farmakes J, Xiao F, Liu G, Chen B, et al. A sulfonated mesoporous silica nanoparticle for enzyme protection against denaturants and controlled release under reducing conditions. *J Colloid Interface Sci.* 2019a;556:292-300.
- Li M-M, Tang Y-Q, Gong Y-F, Cheng W, Li H-L, Kong F-E, et al. Development of an oncogenic dedifferentiation SOX signature with prognostic significance in hepatocellular carcinoma. *BMC Cancer.* 2019b;19:851-61.
- Liu H, Sun H, Zhang B, Liu S, Deng S, Weng Z, et al. 18 F-FDG PET imaging for monitoring the early anti-tumor effect of albendazole on triple-negative breast cancer. *Breast Cancer.* 2020;27:372-80.
- Liu M, Zhang X, Yang B, Deng F, Ji J, Yang Y, et al. Luminescence tunable fluorescent organic nanoparticles from polyethyleneimine and maltose: facile preparation and bioimaging applications. *RSC Adv.* 2014;4:22294-8.
- Mahmood Y, Khan IU, Shahzad Y, Khan RU, Khalid SH, Yousaf AM, et al. Amino-decorated mesoporous silica nanoparticles for controlled sofosbuvir delivery. *Eur J Pharm Sci.* 2020;143:105184.
- Maleki A, Kettiger H, Schoubben A, Rosenholm JM, Ambrogi V, Hamidi M. Mesoporous silica materials: From physico-chemical properties to enhanced dissolution of poorly water-soluble drugs. *J Control Release.* 2017;262:329-47.
- Marzbani B, Nazari J, Najafi F, Marzbani B, Shahabadi S, Amini M, et al. Dietary patterns, nutrition, and risk of breast cancer: a case-control study in the west of Iran. *Epidemiol Health.* 2019;41:e2019003.
- Mehmood A, Ghafar H, Yaqoob S, Gohar UF, Ahmad B. Mesoporous silica nanoparticles: a review. *J Develop Drugs.* 2017;6:1000174.
- Momenimovahed Z, Salehiniya H. Epidemiological characteristics of and risk factors for breast cancer in the world. *Breast Cancer.* 2019;11:151-64.
- Movahedi F, Ebrahimi Shahmabadi H, Alavi SE, Koochi Moftakhari Esfahani M. Release modeling and comparison of nanoarchaeosomal, nanoliposomal and pegylated nanoliposomal carriers for paclitaxel. *Tumor Biol.* 2014;35:8665-72.
- Nguyen CT, Webb RI, Lambert LK, Strounina E, Lee EC, Parat M-O, et al. Bifunctional succinylated ϵ -polylysine-coated mesoporous silica nanoparticles for pH-responsive and intracellular drug delivery targeting the colon. *ACS Appl Mater Interfaces.* 2017;9:9470-83.
- Noorani L, Stenzel M, Liang R, Pourgholami MH, Morris DL. Albumin nanoparticles increase the anticancer efficacy of albendazole in ovarian cancer xenograft model. *J Nanobiotechnology.* 2015;13:25.

- Pandey PK, Sharma AK, Rani S, Mishra G, Kandasamy G, Patra AK, et al. MCM-41 nanoparticles for brain delivery: better choline-esterase and amyloid formation inhibition with improved kinetics. *ACS Biomater Sci Eng*. 2018;4:2860-9.
- Patel K, Doudican NA, Schiff PB, Orlow SJ. Albendazole sensitizes cancer cells to ionizing radiation. *Radiat Oncol*. 2011;6:160-6.
- Pavan Kumar M, Madhusudan Rao Y, Apte S. Improved bioavailability of albendazole following oral administration of nanosuspension in rats. *Curr Nanosci*. 2007;3:191-4.
- Porta-i-Batalla M, Eckstein C, Xifré-Pérez E, Formentín P, Ferré-Borrull J, Marsal LF. Sustained, controlled and stimuli-responsive drug release systems based on nanoporous anodic alumina with layer-by-layer polyelectrolyte. *Nanoscale Res Lett*. 2016;11:372-80.
- Pourgholami M, Woon L, Almajd R, Akhter J, Bowery P, Morris D. In vitro and in vivo suppression of growth of hepatocellular carcinoma cells by albendazole. *Cancer Lett*. 2001;165:43-9.
- Rabinel P, Dousse D, Muscari F, Suc B. Management of liver cancer. The Surgeon's point of view. *Rep Pract Oncol Radiother*. 2017;22:176-80.
- Rahikkala A, Pereira SA, Figueiredo P, Passos ML, Araújo AR, Saraiva MLM, et al. Mesoporous silica nanoparticles for targeted and stimuli-responsive delivery of chemotherapeutics: A review. *Adv Biosys*. 2018;2:1800020.
- Ramezani Farani M, Khadive Parsi P, Riazi G, Shafiee Ardestani M, Saligeh Rad H. Extending the application of a magnetic PEG three-part drug release device on a graphene substrate for the removal of Gram-positive and Gram-negative bacteria and cancerous and pathologic cells. *Drug Des Devel Ther*. 2019;13:1581-91.
- Ramezani Farani M, Khadiv-Parsi P, Riazi GH, Shafiee Ardestani M, Saligeh Rad H. PEGylation of graphene/iron oxide nanocomposite: assessment of release of doxorubicin, magnetically targeted drug delivery and photothermal therapy. *Appl Nanosci*. 2020;10:1205-17.
- Raza A, Sime FB, Cabot PJ, Maqbool F, Roberts JA, Falconer JR. Solid nanoparticles for oral antimicrobial drug delivery: A review. *Drug Discov Today*. 2019;24:858-66.
- Savio E, Dominguez L, Malanga A, Quevedo D, Saldana J, Camarote C, et al. Lipidic matrix of albendazole: an alternative for systemic infections. *Boll Chim Farm*. 1998;137:345-9.
- Shahabi J, Ebrahimi Shahmabadi H, Alavi SE, Movahedi F, Koohi Moftakhari Esfahani M, Zadeh Mehrizi T, et al. Effect of gold nanoparticles on properties of nanoliposomal hydroxyurea: an in vitro study. *Indian J Clin Biochem*. 2014;29:315-20.
- Syned NbHM. Microstructural studies of strontium titanate ceramic pressed at varying pressure. Skudai, Johor Bahru, Johor: Malaysia Universiti Teknologi, Thesis, 2014.
- Tawfeek GM, Baki MHA, Ibrahim AN, Mostafa MAH, Fathy MM, Diab MSED. Enhancement of the therapeutic efficacy of praziquantel in murine Schistosomiasis mansoni using silica nanocarrier. *Parasitol Res*. 2019;118:3519-33.
- Tzankova V, Aluani D, Yordanov Y, Valoti M, Frosini M, Spassova I, et al. In vitro toxicity evaluation of lomefloxacin-loaded MCM-41 mesoporous silica nanoparticles. *Drug Chem Toxicol*. 2019;44:238-49.
- Vazhayal L, Talasila S, Abdul Azeez PM, Solaiappan A. Mesochanneled hierarchically porous aluminosiloxane aerogel microspheres as a stable support for pH-responsive controlled drug release. *ACS Appl Mater Interfaces*. 2014;6:15564-74.
- Yao Y, Zhang M, Shi J, Gong M, Zhang H, Yang Y. Encapsulation of fluorescein into MCM-41 mesoporous molecular sieve by a sol-gel method. *Mater Lett*. 2001;48:44-8.
- Zeleňák V, Halamová D, Almáši M, Žid L, Zeleňáková A, Kapusta O. Ordered cubic nanoporous silica support MCM-48 for delivery of poorly soluble drug indomethacin. *Appl Surf Sci*. 2018;443:525-34.